Sound & Vibration 2025, 59(3), 2315.
https://doi.org/10.59400/sv2315

Article

A new Helmholtz type sonic crystal for wide-band sound attenuation

Javad Goodini, Davood Younesian*

School of Railway Engineering, Iran University of Science and Technology, Tehran 16846-13114, Iran
*** Corresponding author:** Davood Younesian, Younesian@iust.ac.ir

CITATION

Goodini J, Younesian D. A new Helmholtz type sonic crystal for wide-band sound attenuation. Sound & Vibration. 2025; 59(3): 2315. https://doi.org/10.59400/sv2315

ARTICLE INFO

Received: 18 December 2024
Accepted: 3 June 2025
Available online: 6 June 2025

Abstract: In this paper, a Helmholtz shape sonic crystal is proposed for bandgap realization and sound attenuation. Using Bloch's theory, bandgap properties of the sonic crystal are investigated for the primitive design of the unit-cell. A geometrical parametric study is implemented for the unit-cell to present its potential in creating bandgaps over the low-frequency range, and an optimization is applied to find its best design according to the low-frequency objective function. A frequency analysis and experimental tests are used to verify the calculated bandgaps from Bloch's theory and to confirm the sound attenuation ability of the proposed design. It is shown that the present design not only creates wide bandgap frequencies in the low-frequency range but also, due to the Helmholtz shape of the unit-cell, provides significant sound attenuation.

Keywords: sonic crystal; bandgap; sound attenuation; optimization; Helmholtz unit-cell

1. Introduction

With the increase in speed and interest in high-speed transportation systems, the solutions for sound and noise pollution have become more prominent. Sonic crystals (SCs) have been suggested as a new method for the solution of noise pollution from transportation systems, particularly for railway vehicles. Their periodic structure, consisting of scatterers placed in fluid media, creates several bandgap frequencies, i.e., the frequency range over which the propagation of acoustic waves is stopped. Sonic crystals are effective in attenuating various types of noise on these specific bandgap frequencies [1,2]. Traditional noise control methods usually suffer from several limitations, such as bulky weights as well as huge scales and failure to provide desired attenuation levels. However, sonic crystals, due to the bandgap feature, can significantly reduce noise levels, making them a promising alternative to conventional methods [3–5]. The recent developments in sonic crystals indicate that they are a viable and effective solution for noise attenuation in transportation systems [6–9].

Sonic crystals have been exploited in various applications during the last decade. Radosz [4] investigated sonic crystals integrated with resonant elements through both numerical simulations and experimental measurements. The study demonstrated sound insulation levels of up to 16 dB, confirming the effectiveness of sonic crystals in noise reduction. Torres et al. [10] introduced Sonic Crystal Acoustic Screens (SCAS) as a novel type of acoustic barrier to attenuate noise from transport infrastructures. Experimental tests revealed a 42% reduction in sound control ability compared to classical barriers, highlighting their potential to compete with conventional acoustic barriers in urban noise control. Alagoz [11] studied the acoustic filtering effect of sonic crystals in space and frequency domain, focusing on a triangular flat lens. He demonstrated that SCs' flat lenses can significantly enhance

specific frequency components emitted from point sources, making SCs act as narrow-band filters and sensitive acoustic detectors. Sánchez-Dehesa and Torrent [12] utilized two-dimensional sonic crystals composed of elastic cylinders in the air to design broadband gradient index lenses. Using a similar structure made from solid cylinders combined with aerogel cylinders, they fabricated a gradient index sonic lens with the ability to tune sound velocity and density by exploiting the elastic properties of the materials [13]. Sonic crystals were used by Bühling et al. [14] to control jet flow direction. It was shown that sonic crystals can redirect the ultrasonic pulses away from the jet axis, showing that SCs are able to reshape ultrasonic fields.

Bandgap properties of SCs are significantly influenced by their design. Multi-resonant scatterers made from two coaxial shells with slits and perforations were investigated as sonic crystals by Mohapatra et al. [15]. By use of simulations and experimental validation, it was demonstrated that the resonance band of the outer shell and inner shell can be used for adjusting the bandgap frequency ranges of the SC. Chen et al. introduced acoustic topological insulators (ATIs) that utilize sonic crystals (SCs) to create multiband topological interface states within wide bandgaps. They suggested such a design for suggesting promising applications in multiband information processing and communication technologies [16]. A novel design of a radial sonic crystal composed of a periodic arrangement of scatterers was introduced by Gupta et al. [17]. The presence of bandgaps within this structure provided a high sound attenuation of approximately 30 dB. Using an optimized polyhedral sonic crystal, Tajsham et al. [18] achieved the noise attenuation of up to 30 dB within the bandgap frequencies and the bandgap coverage factor of 179.01% over the investigated frequency range of 0–6 kHz. Shakouri et al. [19] demonstrated that hierarchical sonic crystals, composed of rotated square inclusions, can confine acoustic energy across a broad frequency range due to Bragg scattering effects. Experimental and computational analyses confirmed the strong acoustic energy confinement of their design with potential application in wave manipulation and acoustic imaging.

Using Sonic crystals, Espinosa et al. [20] investigated negative refraction and focusing of acoustic waves in steel rods arranged in a square lattice in a water matrix. Identification of negative refraction and calculation of band structures were extracted using the plane wave expansion (PWE) method. Moreover, the extraction of negative refraction for steel rods in water structure was experimentally investigated by Ke et al. [21] . The authors used a point source to generate acoustic waves and measured the pressure field behind the crystal. Similarly, experimental demonstrations of negative refraction and zero-index properties using a two-dimensional acoustic metamaterial have been reported by Zheng et al. [22]. The researchers fabricated the metamaterial sample and measured the pressure field behind it to confirm the negative refraction effect. The formation of acoustic band gaps in two-dimensional locally resonant sonic crystals was studied by Chalmers et al. [23]. This study investigated the influence of the tube arrangement and properties on the band gap formation, while the steel tubes (acting as scatterers) were modelled as fluid inclusions with high stiffness and mass. The design of SCs composed of cylindrical rods for noise attenuation using numerical simulations was reported by Lee et al. [24]. The authors explored the effects of different parameters such as lattice constant and material properties on the SCs performance.

Using optimization methods is an effective tool for improving bandgap frequencies and attenuation properties of metamaterials [25]. Jia et al. employed a topology optimization algorithm to maximize the sound attenuation properties of SCs. Using the optimized unit-cell designs and band structures, enhanced spatial decay of evanescent waves was achieved over bandgaps [26]. Lee et al. [27] proposed a window using locally resonant sonic crystals (LRSC) for noise attenuation. The Taguchi method was used to determine the optimal geometric parameters of the LRSC window for achieving the best noise reduction performance. A topology optimization approach for designing acoustic Dirac cones and topological insulators was suggested by Dong et al. [28]. The authors employed a two-step bottom-up topology optimization process to achieve this goal.

Recently, the Helmholtz resonator has been integrated into the design of sonic crystals to improve sound attenuation or provide new features in SC. The integration of Helmholtz resonators (HRs) into sonic crystal noise barriers (SCNBs) for enhanced low-frequency noise attenuation was explored by Redondo et al. [29]. The results showed that facing the Helmholtz resonator entrance with the incident wave direction leads to increased insertion loss above the Bragg band gap. Li et al. explored the band structures and their tuning in metamaterials using Helmholtz resonators, and they reported the importance of Helmholtz resonant frequency for achieving optimal performance of the crystal [30]. Han et al. presented a novel Helmholtz-type crystal for low-frequency noise reduction [31]. The study employed FEM and transfer matrix method (TMM) simulations to calculate the bandgap diagram of the crystal. Wave propagation in a 2D sonic crystal with a Helmholtz resonant defect was examined by Wu et al. [32]. The key finding of this study was that the frequencies of the defect band are strongly dependent on the geometry of the resonator defect. Yang et al. proposed an acoustic energy harvester that combines the resonant structure of a sonic crystal resonator (SCR) with an electromechanical Helmholtz resonator incorporating a piezoelectric composite diaphragm [33]. This coupled structure aims to enhance energy harvesting by improving the acoustic resonance coupling between the crystal and the defect.

By reviewing the state of the art in the field of sonic crystals, we can see that they are significantly effective in controlling and attenuating sound waves. The unit-cell design plays a critical role in determining the BG properties and performance of sonic crystals. More recently, the employment of Helmholtz resonators in sonic crystals has started as a promising approach for enhancing performance of sonic crystals. Optimization methods have been used as an efficient tool in the context of SCs to design unit-cells or to enhance the topology of the cell, leading to improved sound attenuation properties.

In this work, we introduce a Helmholtz-type sonic crystal that incorporates eight Helmholtz resonators arranged symmetrically within a single unit cell. Unlike previous designs, many of which rely on simpler resonator configurations or target limited frequency ranges [4,15,29], our structure is optimized using a genetic algorithm to enhance sound attenuation across a broader low-frequency band (below 6000 Hz). This approach yields a total bandgap summation (BGS) of 3425 Hz, representing a significant improvement in wide-band acoustic performance. The

effectiveness of the design is supported by both numerical simulations and experimental validation.

2. Unit-cell design

In this section, the novel sonic unit-cell, schematically illustrated in **Figure 1,** is introduced and its bandgap properties are calculated. The unit-cell is made of a Helmholtz-shaped scatterer placed in the fluid background medium, which is air in this research. The initial idea of the unit-cell is inspired by the well-known Helmholtz resonator which is widely used in the context of noise control. The design starts with drawing a circle with a radius R in a square with the length "a". Then, we draw half of the resonator using the key points named 1 to 6. The half geometry is mirrored around the vertical axes to complete one resonator. Finally, eight identical resonators are arranged symmetrically around the circumference of the circle. All the internal edges of the 8 resonators are smoothed using a 0.001 [m] fillet. By removing the 8 resonators from the base circle, the final geometry for the Helmholtz shaped novel unit-cell is achieved. In the design of unit-cell, 6 key points with the coordinates (0,R), (a_1,R), (a_2,R), (a_3,R), (a_4,R), (a_5,R) are utilized. These coordinates can be used to control the geometry of the unit-cell. The primitive values for the coordinates of these points are listed in **Table 1**.

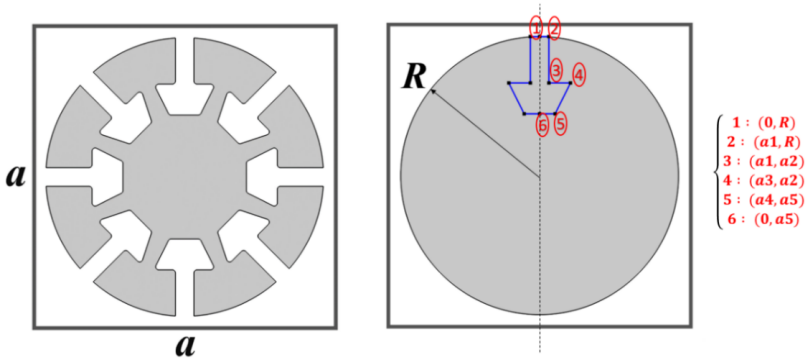

Figure 1. Schematic of the unit-cell and key coordinates.

Table 1. Parameters of the primitive unit-cell.

Parameter	a	R	a_1	a_2	a_3	a_4	a_5
Value	0.1 [m]	0.045 [m]	0.003 [m]	0.03 [m]	0.01 [m]	0.005 [m]	0.02 [m]
Description	Unit-cell size	Scatterer radius	Coordinate of Resonator	Coordinate of Resonator	Coordinate of Resonator	Coordinate of Resonator	Coordinate of Resonator

The evaluation of bandgaps is implemented using Bloch's theorem; according to this theory, an infinite periodic structure can be replaced by its smallest repeated micro-structure called unit-cell. By moving the wave vector around the irreducible Brillouin zone of the cell, the bandgap diagram can be achieved for the primitive unit-cell and it can be extended to the infinite structure due to the periodicity. The bandgap diagram (known as the dispersion diagram) provides enough information about the frequencies over which a bandgap exists.

In here, the finite element method is implemented using COMSOL Multiphysics 6.1©, and the corresponding bandgap diagram is evaluated and presented here. This calculation employs the PWE (plane wave expansion) technique along with the periodic Floquet-Bloch boundary condition presented by

$$\tilde{\boldsymbol{p}}(\boldsymbol{r}+\boldsymbol{a}) = \tilde{\boldsymbol{p}}(\boldsymbol{r})\boldsymbol{e}^{\boldsymbol{ika}} \tag{1}$$

where, $\tilde{p}(\boldsymbol{r})$ is a periodic function with the periodicity length of "a" that is the same periodicity length of the sonic crystal. $\boldsymbol{k}$ is the wave vector and $\boldsymbol{r}$ is the position vector.

The material of the background medium is air and the chosen material for the scatterer is PLA.

As is typical for sonic crystals functioning in air, the PLA scatterers are assumed to be acoustically stiff in the numerical simulations [6,23]. Because PLA's stiffness, which is represented in its high sound speed (1860 m/s) relative to air's (343 m/s), makes its elastic response insignificant in this situation, this simplification enables us to concentrate on the geometric aspects impacting bandgap generation and sound attenuation.

The irreducible Brillouin zone and the edge points of Γ, X, M are presented for the unit-cell in **Figure 2**. By moving the wave vector across the Brillouin zone and solving the related eigenvalue problem, the bandgap diagram can be evaluated. This diagram is depicted in **Figure 2** while eight bandgaps are appear on the frequency range of 0–10 kHz. The details of bandgap frequencies including opening frequency, closing frequency, and bandgap width are presented in **Table 2**.

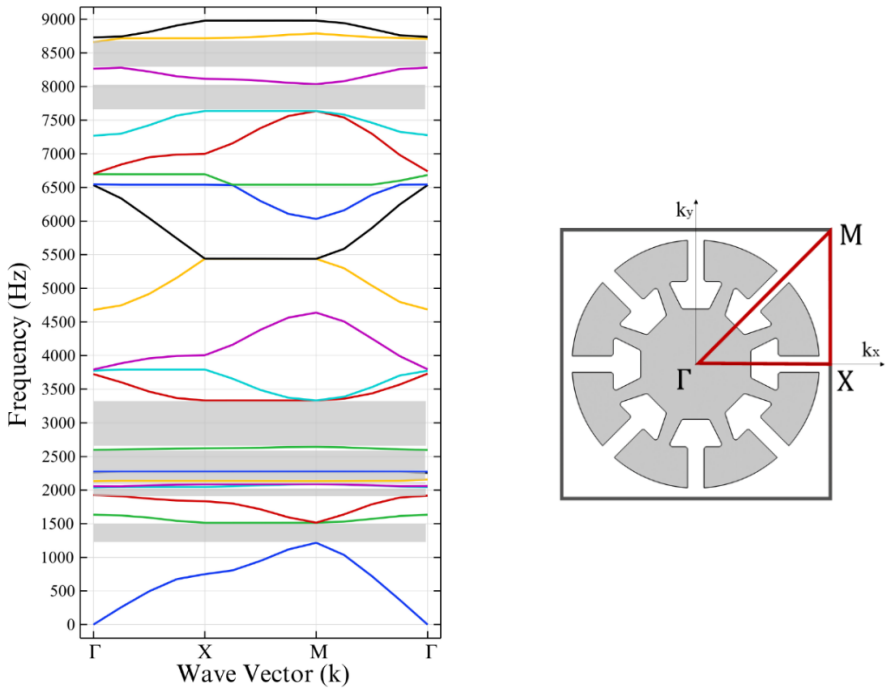

(a) **(b)**

Figure 2. (a) Bandgap diagram of the primitive unit-cell **(b)** Irreducible Brillouin zone.

Table 2. Details of the bandgap frequencies of the primitive unit-cell.

Bandgap number	Opening freq.	Closing freq.	Width
1st	1217 Hz	1515 Hz	298 Hz
2nd	1860 Hz	2046 Hz	186 Hz
3rd	2055 Hz	2133 Hz	78 Hz
4th	2133 Hz	2265 Hz	132 Hz
5th	2275 Hz	2597 Hz	332 Hz
6th	2642 Hz	3332 Hz	690 Hz
7th	7636 Hz	8035 Hz	399 Hz
8th	8277 Hz	8673 Hz	396 Hz

The Brillouin zone is the primitive cell in the reciprocal lattice of the periodic structure. For our square lattice sonic crystal with lattice constant a = 0.1 m, the irreducible Brillouin zone is a triangular region defined by the points Γ(0,0), X(π/a,0) and M(π/a,π/a), as shown in **Figure 2b**. Sweeping the wave vector across this zone via the plane wave expansion method reveals the bandgap frequencies. The material properties of the unit cell are presented in **Table 3**.

Table 3. Material properties of the primitive unit-cell.

Materials	Speed of sound (C)	Density (ρ)
PLA	1860 [m/s]	1240 [kg/m^3]
Air	343 [m/s]	1.293 [kg/m^3]

3. Parametric study

This section investigates the influence of key parameters on the summation bandgaps (BGS) within the low-frequency range, defined as below 6000 Hz. In all cases, BGS is evaluated and plotted as a function of parameters a_1 and a_2.

The BGS is defined as the total width of all bandgaps within the frequency range of interest (< 6000 Hz), calculated as $\sum_k (f_{\text{closing}} - f_{\text{opening}})_k$. A higher BGS indicates greater noise attenuation potential over a broader low-frequency range. **Figure 3** presents the BGS as a function of a_1 and a_2 for three different values of a_3 (0.01, 0.05, and 0.075 m). The results show a consistent trend: BGS increases with increasing a_1 across all three a_3 values, indicating a clear and direct influence of a_1 on the bandgap behavior.

The same trend is observed for a_2 in the cases of a_3 = 0.01m, i.e., the BGS increases with the increase of a_1. However, as the parameter of a_3 increases to higher values of 0.05 and 0.075 m, the impact of a_2 on BGS becomes less significant, and the effects of parameters a_1 and a_3 become more dominant. Overall, a_1 exhibits strong positive sensitivity to BGS, consistently leading to wider bandgaps with increasing values. While a_2 also shows a positive influence at lower a_3 values, its effect becomes less significant as a_3 increases. In contrast, the influence of a_3 itself weakens at higher values, likely due to competing geometric interactions. The contour plots use a color range from dark blue (low BGS) to light blue (high BGS), where a higher BGS signifies greater noise attenuation potential over a broader low-frequency range. The

influence of a_2 on BGS varies with other parameters, lacking a universal trend. Specifically, while a_1 consistently increases BGS, a_2's effect depends on a_3, a_4, and a_5, as seen in **Figures 3**–**5**.

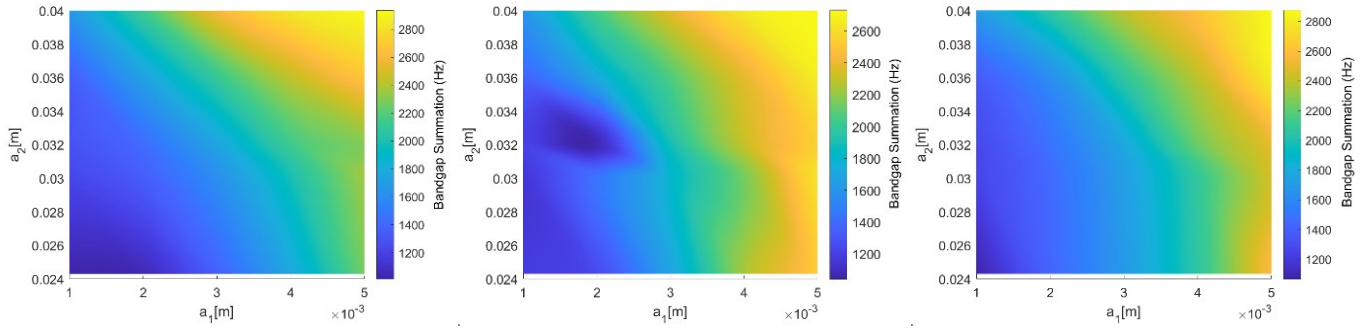

(a) a_3 = 0.01 m **(b)** a_3 = 0.05 m **(c)** a_3 = 0.075 m

Figure 3. Variation of BGS with a_1 and a_2 for **(a)** a_3 = 0.01 m, **(b)** a_3 = 0.05, and **(c)** a_3 = 0.075. Colors range from dark blue (low BGS) to light blue (high BGS). The non-continuous dark blue region in **(b)** results from a complex interaction: as a_3 increases, it starts to offset the influence of a_2, which disrupts the continuity of the bandgap and leads to its fragmentation.

The variations of BGS with respect to a_1 and a_2 and for three different values of a_4 = 0.002, 0.003, and 0.00425 m are plotted in **Figure 4**. Generally, for these investigated values of a_4, the BGS increases with increasing both a_1 and a_2. Regarding parameter a_4, the BGS reaches values of 3000 Hz for a_4 = 0.002 and 0.003 m. However, in the case of a_4 = 0.00425 m, the BGS reaches 2800 Hz in the maximum at last.

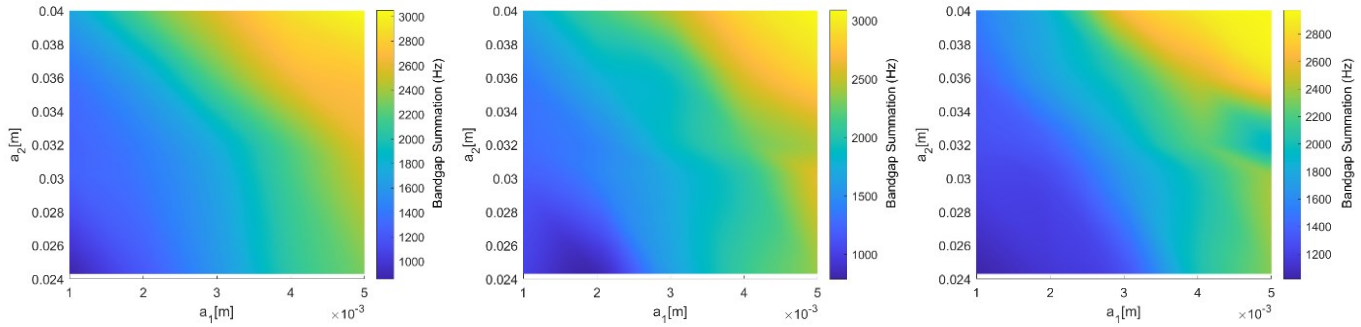

(a) a_4 = 0.02 m **(b)** a_4 = 0.00275 m **(c)** a_4 = 0.00425 m

Figure 4. Variation of BGS with a_1 and a_2 for **(a)** a_4 = 0.002 m, **(b)** a_4 = 0.003 m, and **(c)** a_4 = 0.00425 m. The light blue region below the orange in **(c)** reflects a local BGS reduction due to narrower bandgaps at higher a_4, suggesting an optimal a_4 range around 0.003 m for maximizing BGS.

Finally, the key parameter of a_5 is changed from a_5 = 0.013 m to a_5 = 0.017 m and a_5 = 0.024 m and the simultaneous variation of BGS is plotted versus a_1 and a_2 in **Figure 5**. We can see that the maximum achieved value for the BGS is around 2300 Hz for a_5 = 0.013 m, it is around 2800 Hz for a_5 = 0.017 and it is around 3000 Hz for a_5 = 0.024 m. Accordingly, it is expected that the BGS increases with increasing a_5. The impact of a_1 on the BGS is again the same as in the cases presented in **Figure 4** and **Figure 5**, i.e., a higher value of a_1 leads to a higher BGS. However, for the

influences of the key parameter of a_2 on BGS, it is not possible to find a general statement, since it has a rather complicated impact on BGS.

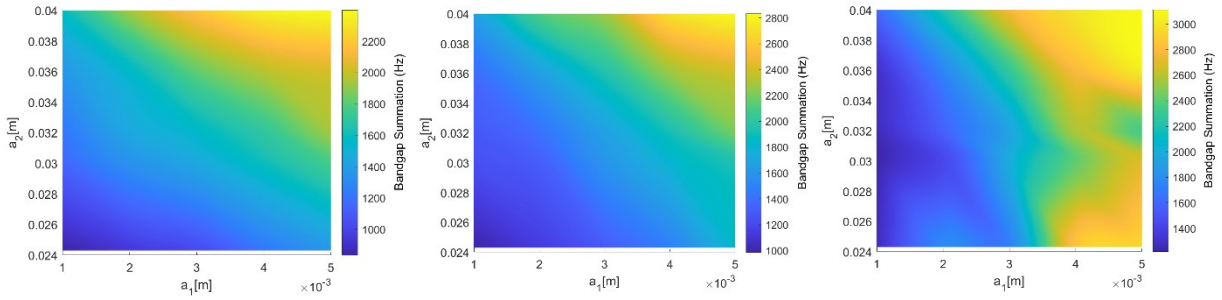

(a) a_5 = 0.0135 m **(b)** a_5 = 0.017 m **(c)** a_5 = 0.024 m

Figure 5. Variation of bandgap summation of the unit-cell with **(a)** a_5 = 0.013 m, **(b)** a_5 = 0.017 m, and **(c)** a_5 = 0.024 m.

In conclusion, this parametric study provides insights into how the key parameters, namely a_1, a_2, a_3, a_4, and a_5, affect the summation bandgaps (BGS) within the low-frequency range (under 6000 Hz). The findings indicate that certain parameters, such as a_1, generally result in an increase in BGS, others, such as a_2, show more complex behavior influenced by the values of parameters a_1, a_3, etc. These variations suggest the complex dependency of the BGS on the key parameters.

The complexity of these interactions shows the need for an optimization process. Such a procedure is essential to determine the optimal combination of parameters that will maximize BGS. Such a design will be more efficient and effective to achieve the desired performance in the low-frequency range. This optimization is addressed in the next section.

4. Optimization

By use of genetic algorithm (GA), the unit-cell's geometry is optimized in this section. The goal is to optimize the geometric parameters a_1 to a_5 to maximize BGS in the low-frequency range (< 6000 Hz) while the length of the unit-cell is fixed to a = 10 cm. The optimization variables and their limits are presented in **Table 4**. The summation of bandgaps over the frequency range of 0–6 kHz is taken as the objective function which is presented in Equation (2).

$$Obj.fun = -\sum_{k}\left(f_{closoing} - f_{opening}\right)_k, freq < 6000 \text{ Hz} \tag{2}$$

In the genetic algorithm, uniform mutation refers to a mutation operator that randomly changes the values of genes, parameters a_1 to a_5, within their allowed ranges using a uniform distribution. This helps promote exploration of the design space. Each gene in a selected chromosome corresponds to a specific parameter value for a potential unit-cell configuration.

A random initial population size equal to 100 is generated for starting the optimization problem which ensures suitable diverse selections at the first generation. Through the selection method named "selection tournament", the population is sorted and the parents for the next generation are selected. In the following step, the "mutation uniform" option is used to introduce mutations that modify certain genes in

a chosen chromosome to explore new areas within the search space. The optimization problem is completed with the stop criteria which is chosen to be 100 iterations.

Genetic algorithm, as a powerful tools in the SC field, search for the optimal solution within the entire design space. GA dispossesses the optimization process from trapping on local optimums. This feature is principally beneficial in the present study, where the design variables affect bandgap properties in a complicated manner [34–37].

Genetic algorithms (GAs) are evolutionary optimization techniques inspired by natural selection, iteratively evolving a population of candidate solutions through selection, crossover, and mutation to maximize an objective function. Here, GA optimizes the unit-cell parameters to maximize BGS, defined as Equation (2).

Table 4. Optimization parameters and their limits.

parameter	Lower bound [m]	Upper bound [m]
a_1	0.001	0.005
a_2	0.0243	0.04
a_3	0.001	0.075
a_4	0.002	0.0035
a_5	0.01	0.024

The convergence diagram of the optimization process is depicted in **Figure 6**. We can see that the 100 iterations are large enough for the optimization process to achieve a satisfactory convergence.

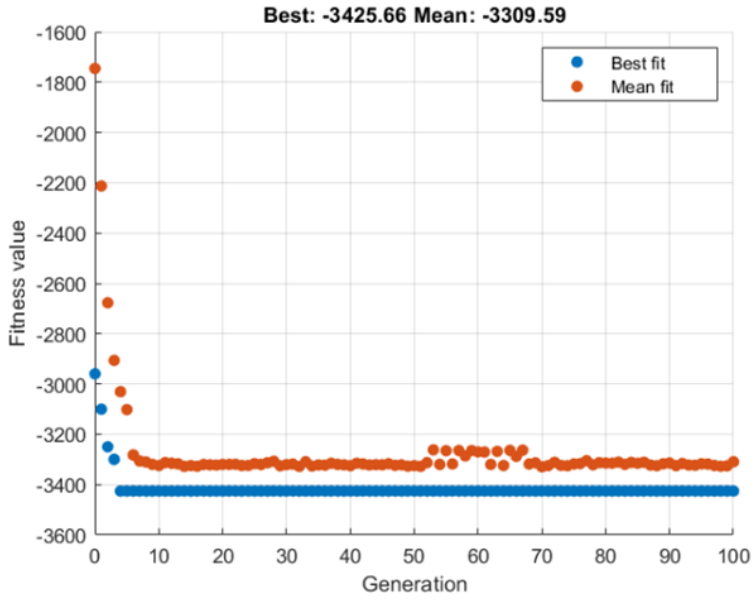

Figure 6. Convergence of the objective function versus generation, showing 'Best fit' (maximum BGS) and 'Mean fit' (average BGS). The hill in Mean fit between generations 50–70 reflects a temporary increase in average population fitness as GA explores a new region of the parameter space before converging.

According to the defined optimization problem, the geometry depicted in **Figure 7a** is achieved for the Helmholtz shape unit-cell. Comparing the geometry of the optimized design with the primitive design, we can see that the optimization method makes the neck length of Helmholtz resonators smaller and it makes the opening area of resonators larger. A More careful comparison can be made between the key parameters of the optimized design (**Table 5**) and the primitive design (**Table 1**). This shows that a_1 and a_2 are increased from initial values while a_3, a_4 and a_5 are decreased from the initial values.

The bandgap diagram related to the optimized design is presented in **Figure 7b**. We can see that eight bandgaps appear below 6000 Hz in the optimized design. The first bandgap is over 1281–1712 Hz, the second one is 2420–2695 Hz, the third one is 2816–3054 Hz, the fourth bandgap is 3054–3503 Hz, and the fifth one is 3561–3889 Hz. The sixth and seventh ones are on 3927–4408 Hz and 4414–4690 Hz, respectively, and the last BG over the considered frequency range is 4768–5715 Hz. Their summation is equal to the value achieved from the optimization algorithm which is 3425 Hz.

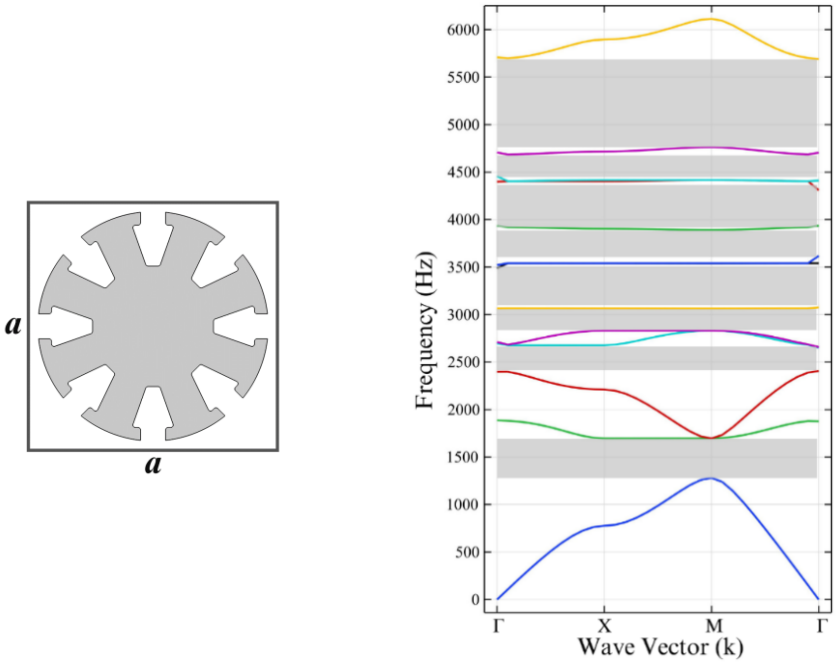

(a) **(b)**

Figure 7. Optmal performance of the proposed unit-cell: (a) Illustration of the optimized geometry and **(b)** related bandgap diagram.

Table 5. Parameters of the optimized unit-cell.

Parameter	a_1	a_2	a_3	a_4	a_5
Value	0.0049026652 [m]	0.0396781724 [m]	0.0082916310 [m]	0.0026599664 [m]	0.0236328652 [m]

It is interesting to compare the optimization results with the parametric study findings. Such comparison also highlights the effectiveness of the genetic algorithm in improving the design for optimal bandgap summation (BGS). In the parametric study, it was observed that increasing a_1 generally led to a higher BGS. Reflecting this

trend, the optimization has pushed a_1 near to its upper bound (0.005 m), as its final value from the optimization is found to be 0.0049 m. Similar to a_1, a_2 also showed a positive effect on BGS in the parametric study. The optimization process has increased a_2 to 0.0397 m, nearing its upper limit (0.04 m).

In the parametric study, we saw that a_3 has a strong impact on BGS, however, it seems that its best value is somehow in the middle limits. Therefore, the optimization resulted in the value of 0.0083 m, since this value enables better overall BGS performance across the frequency range. For a_4, the parametric study showed that increasing this value increases BGS, however, BGS decreased slightly at the upper bound. Accordingly, the optimization process returned a moderate value for a_4 as its optimum value is 0.00266 m. Finally, higher values of a_5 increase the value of BGS in the parametric study. Hence, the optimized value of a_5 = 0.0236 m is also close to its upper bound.

5. Numerical and experimental validations

In this section, at first, the numerical investigation using the finite element method is implemented to validate the bandgap frequencies obtained in the last section. We remember that in this research, the bandgaps' performance is the main characteristic of the sonic crystal since the propagating acoustic waves are attenuated on these specific frequencies. This investigation is performed for the optimized unit-cell. In the last sections, the bandgaps are evaluated from Bloch's theory, which is based on an infinite structure. In this section, the analysis is performed for a finite structure.

For the aim of numerical investigation, the schematic illustration presented in **Figure 8** is utilized. To approach the finite model into the infinite one, periodic boundary conditions are applied to the top and bottom edges. The input excitation is considered as a sound pressure with the amplitude of 1 Pa. The receiver is a linear microphone that is placed behind the sonic crystals. Such a microphone minimizes the effects of signal concentration at peak. A boundary condition of a perfectly matched layer (PML) is suggested for the right edge on the side of the microphone which reduces the effects of reflections from boundaries.

The insertion loss (IL) defined in Equation (3) is used to present the result of the frequency analysis.

$$\textbf{Insertion Loss (dB)} = \textbf{SPL2 (dB)} - \textbf{SPL1 (dB)} \tag{3}$$

In this equation, SPL1 is the sound pressure in decibels (dB) measured in the presence of the sonic crystals and SPL2 is the sound pressure in decibels (dB) measured in the absence of the sonic crystals.

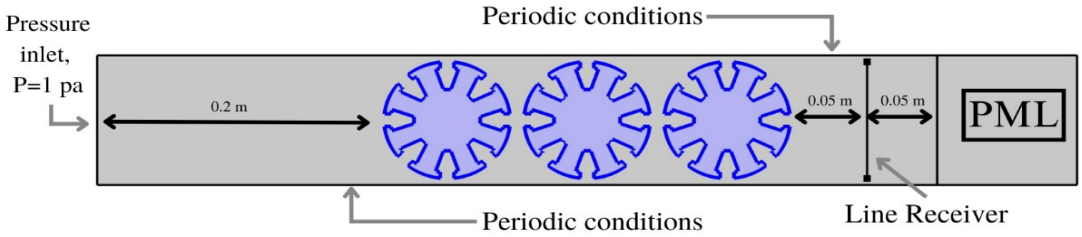

Figure 8. Schematic of the simulated medium.

The frequency analysis result for the optimized design is plotted in **Figure 9** beside the bandgap diagram (BGs are highlighted with grey tapes). Everywhere a bandgap exists, a significant amount of insertion loss (IL) is observed. This confirms the accuracy of the bandgap and frequency studies.

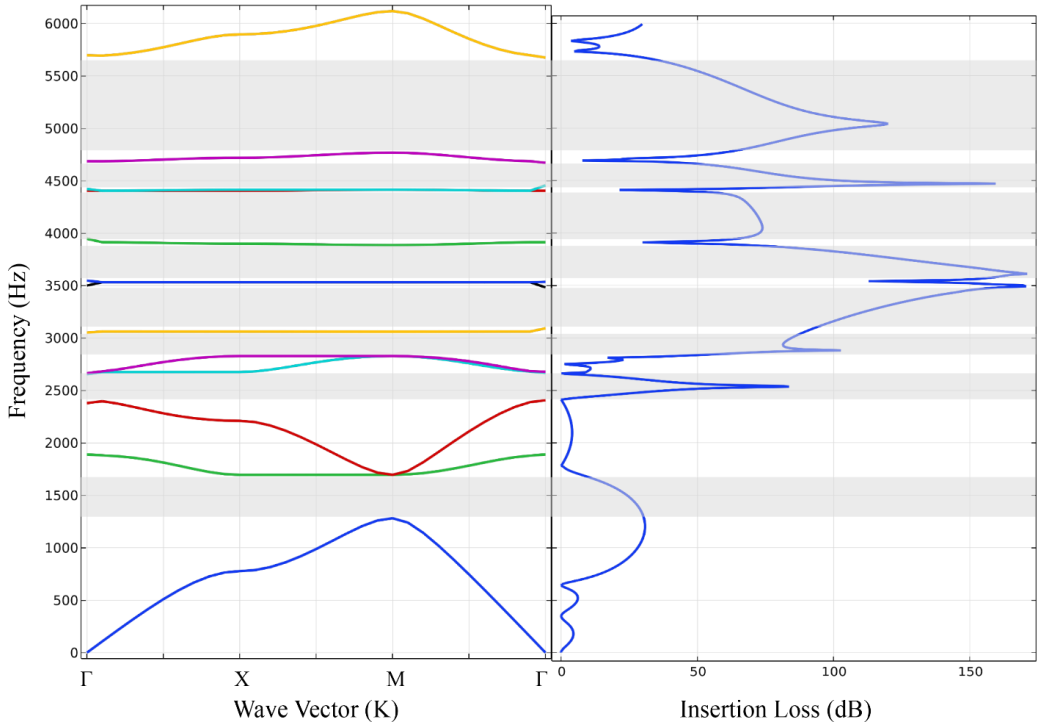

Figure 9. Attenuation diagram for the optimization structure and its comparison with bandgap frequencies.

In order to verify the numerical simulations and investigate the practical application of the sonic crystals concept, an experimental test is conducted. Accordingly, the specimen for experiments is fabricated using 3D printing process and the produced sonic crystal is shown in **Figure 10**. The geometry and size of the fabricated crystal are the same as those one achieved from optimization. The sonic crystal is made from PLA material in 3 × 3 arrays. The experimental setup included a wooden box measuring 95 × 40 × 30 cm^3, with its interior walls lined with 5 cm thick melamine foam to reduce reflections. The box lid was closed during the test to minimize external noise. Although the base was not covered with foam, the setup provided a controlled environment. In the simulations, rigid boundary conditions were assumed, approximating the box but not accounting for foam absorption. Three independent tests were conducted, showing good repeatability with consistent IL peak positions.

Figure 11 shows the experimental setup and the numerical simulation of the experiment environment. The unit-cells are placed on a wooden substrate to remain fixed during the experiments. The height of the sonic crystals is 20 cm, the speaker is placed at 20 cm on the right side of the sonic crystal, and the microphone is placed at 5 cm on the left side of the sonic crystal. The speaker driven by a function generator

serves as the input excitation and the Behringer C-2 microphone serves as the receiver. The microphone is connected to a Focusrite Scarlett 18i20 2nd Gen audio interface for capturing the output signal.

Figure 10. Fabricated model of the unit-cell.

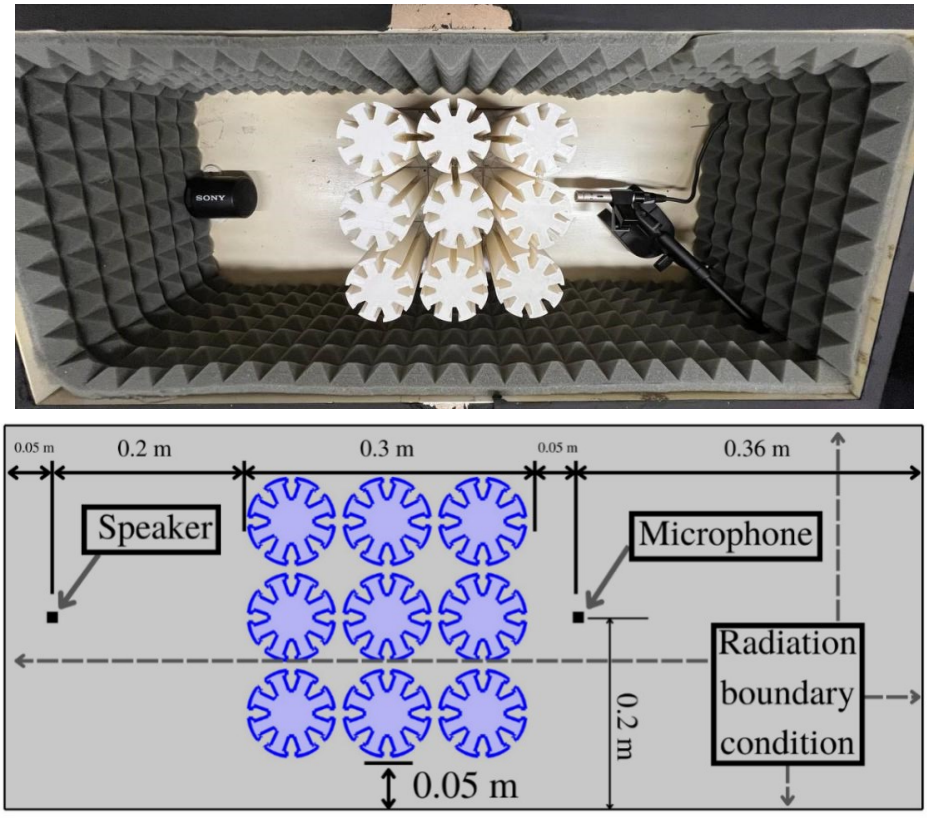

Figure 11. Set up for the experimental test.

Figure 12 compares the numerical frequency analysis over the 0–6000 Hz range with the experimental results. The simulation and the experimental data show a good alignment, with the insertion loss (IL) peaks closely matching in both amplitude and frequency position. The slight variations observed are due to practical experimental considerations such as fabrication tolerances and sound reflections from the wooden

box. These results validate the numerical model and demonstrate the ability of the sonic crystal design to attenuate sound.

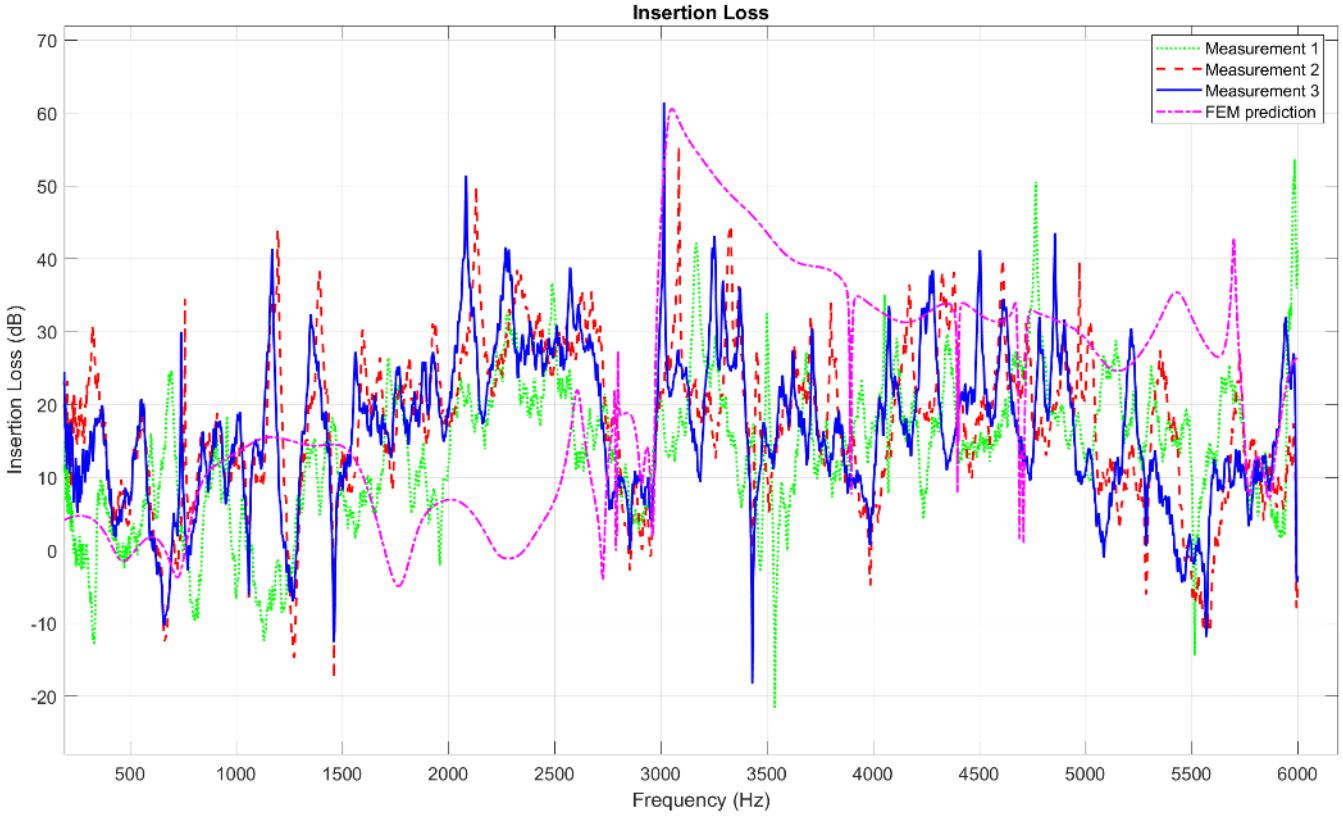

Figure 12. Comparison between IL diagram from experiments and numerical simulation.

6. Conclusions

Sound attenuation properties of a novel sonic crystal unit-cell were studied in this research. The bandgap properties of the cell were calculated from Bloch's theory and the sound attenuation was investigated using frequency analysis as well as experimental tests. A parametric study was implemented for the key geometrical parameters of the cell, while complex behavior from the impact of these geometrical parameters on BG was observed. Accordingly, in the next step, these key parameters were optimized subject to bandgap summation as a low-frequency objective function. The optimization results align well with the key observations from the parametric study, with parameters a_1, a_2, and a_5 reaching close to their upper bounds to maximize BGS, while a_3 and a_4 are optimized to intermediate values to achieve the best design. These results validate the insights from the parametric study and demonstrate that the genetic algorithm successfully searches complex parameter behaviors to identify an optimal configuration for maximum BGS across the target frequency range. The frequency analysis along with experiments was conducted for the optimized design. These findings further confirmed the calculated BG from the first step and also indicated the sound attenuation ability and practical application of the proposed design. The research results show that the new structure has good sound attenuation effect in the low frequency range, up to 56.8 dB.

Author contributions: Conceptualization, DY; methodology, JG; software, JG; validation, JG, and DY; formal analysis, JG; investigation, JG and DY; resources, DY; data curation, DY; writing—original draft preparation, JG; writing—review and editing, DY; visualization, JG; supervision, DY; project administration, DY; funding acquisition, DY. All authors have read and agreed to the published version of the manuscript.

Institutional review board statement: Not applicable.

Informed consent statement: Not applicable.

Conflict of interest: The authors declare no conflict of interest.

References

1. Clark C, Stansfeld SA. The Effect of Transportation Noise on Health and Cognitive Development: A Review of Recent Evidence. International Journal of Comparative Psychology. 2007; 20(2). doi: 10.46867/ijcp.2007.20.02.10
2. Singh N, Davar SC. Noise Pollution-Sources, Effects and Control. Journal of Human Ecology. 2004; 16(3): 181–187. doi: 10.1080/09709274.2004.11905735
3. Mahesh K, Mini RS. Theoretical investigation on the acoustic performance of Helmholtz resonator integrated microperforated panel absorber. Applied Acoustics. 2021; 178: 108012. doi: 10.1016/j.apacoust.2021.108012
4. Radosz J. Acoustic performance of noise barrier based on sonic crystals with resonant elements. Applied Acoustics. 2019; 155: 492–499. doi: 10.1016/j.apacoust.2019.06.003
5. Elford DP, Chalmers L, Kusmartsev FV, Swallowe GM. Matryoshka locally resonant sonic crystal. The Journal of the Acoustical Society of America. 2011; 130(5): 2746–2755. doi: 10.1121/1.3643818
6. Sánchez-Pérez JV, Caballero D, Mártinez-Sala R, et al. Sound Attenuation by a Two-Dimensional Array of Rigid Cylinders. Physical Review Letters. 1998; 80(24): 5325–5328. doi: 10.1103/physrevlett.80.5325
7. Ho KM, Cheng CK, Yang Z, et al. Broadband locally resonant sonic shields. Applied Physics Letters. 2003; 83(26): 5566–5568. doi: 10.1063/1.1637152
8. Martínez-Sala R, Rubio C, García-Raffi LM, et al. Control of noise by trees arranged like sonic crystals. Journal of Sound and Vibration. 2006; 291(1–2): 100–106. doi: 10.1016/j.jsv.2005.05.030
9. Caballero D, Sánchez-Dehesa J, Rubio C, et al. Large two-dimensional sonic band gaps. Physical Review E. 1999; 60(6): R6316.
10. Peiró-Torres MP, Redondo J, Bravo JM, et al. Open Noise Barriers Based on Sonic Crystals. Advances in Noise Control in Transport Infrastructures. Transportation Research Procedia. 2016; 18: 392–398. doi: 10.1016/j.trpro.2016.12.051
11. Alagoz S. An analysis of the spatio-spectral acoustic filtering effect of sonic crystals. Chinese Journal of Physics. 2016; 54(5): 788–794. doi: 10.1016/j.cjph.2016.08.003
12. Sánchez-Dehesa J, Torrent D. A gradient index sonic lens based on acoustic metamaterials. The Journal of the Acoustical Society of America. 2007; 122: 2966–2966. doi: 10.1121/1.2942578
13. Torrent D, Sánchez-Dehesa J. Acoustic metamaterials for new two-dimensional sonic devices. New Journal of Physics. 2007; 9(9): 323–323. doi: 10.1088/1367-2630/9/9/323
14. Bühling B, Maack S, Strangfeld C. Using sonic crystals to separate the acoustic from the flow field of a fluidic transducer. Applied Acoustics. 2022; 189: 108608. doi: 10.1016/j.apacoust.2021.108608
15. Mohapatra K, Jena DP. Insertion loss of sonic crystal made with multi resonant shells. Applied Acoustics. 2021; 171: 107676. doi: 10.1016/j.apacoust.2020.107676
16. Chen Y, An S, Lan Z, et al. Multiband acoustic helical interface states in inverse-designed sonic crystals with glide symmetry. Composite Structures. 2024; 335: 117994. doi: 10.1016/j.compstruct.2024.117994
17. Gupta A, Lim KM, Chew CH. Design of radial sonic crystal for sound attenuation from divergent sound source. Wave Motion. 2015; 55: 1–9. doi: 10.1016/j.wavemoti.2015.01.002
18. Tajsham A, Younesian D, Goodini J, Hosseinkhani A. A new polyhedral sonic crystal for broadband sound barriers: Optimization and experimental study. Applied Acoustics. 2024; 218: 109881. doi: 10.1016/j.apacoust.2024.109881

19. Shakouri A, Xu F, Fan Z. Broadband acoustic energy confinement in hierarchical sonic crystals composed of rotated square inclusions. Applied Physics Letters. 2017; 111(5). doi: 10.1063/1.4985230
20. spinosa V, Sánchez-Morcillo VJ, Staliunas K, et al. Subdiffractive propagation of ultrasound in sonic crystals. Physical Review B. 2007; 76(14). doi: 10.1103/physrevb.76.140302
21. Ke M, Liu Z, Qiu C, et al. Negative-refraction imaging with two-dimensional phononic crystals. Physical Review B. 2005; 72(6). doi: 10.1103/physrevb.72.064306
22. Zheng LY, Wu Y, Ni X, et al. Acoustic cloaking by a near-zero-index phononic crystal. Applied Physics Letters. 2014; 104(16). doi: 10.1063/1.4873354
23. Chalmers L, Elford DP, Kusmartsev FV, Swallowe GM. Acoustic band gap formation in two-dimensional locally resonant sonic crystals comprised of Helmholtz resonators. International Journal of Modern Physics B. 2009; 23: 4234–4243. doi: 10.1142/s0217979209063390
24. Lee HM, Lim KM, Lee HP. Environmental and sound divergence effects on the performance of rectangular sonic crystals with Helmholtz resonators. Journal of Vibration and Control. 2017; 24(12): 2483–2493. doi: 10.1177/1077546316688422
25. Chen Y, Huang X, Sun G, et al. Maximizing spatial decay of evanescent waves in phononic crystals by topology optimization. Computers & Structures. 2017; 182: 430–447. doi: 10.1016/j.compstruc.2017.01.001
26. Jia Z, Yan Y, Bao Y, et al. Maximizing attenuation of sound waves preserving air permeability in sonic crystals via topology optimization. Applied Acoustics. 2025; 228: 110348. doi: 10.1016/j.apacoust.2024.110348
27. Lee HM, Hua Y, Xie J, Lee HP. Parametric Optimization of Local Resonant Sonic Crystals Window on Noise Attenuation by Using Taguchi Method and ANOVA Analysis. Crystals. 2022; 12(2): 160. doi: 10.3390/cryst12020160
28. Dong HW, Zhao SD, Zhu R, et al. Customizing acoustic dirac cones and topological insulators in square lattices by topology optimization. Journal of Sound and Vibration. 2021; 493: 115687. doi: 10.1016/j.jsv.2020.115687
29. Redondo J, Ramírez-Solana D, Picó R. Increasing the Insertion Loss of Sonic Crystal Noise Barriers with Helmholtz Resonators. Applied Sciences. 2023; 13(6): 3662. doi: 10.3390/app13063662
30. Li JB, Wang YS, Zhang C. Tuning of Acoustic Bandgaps in Phononic Crystals With Helmholtz Resonators. Journal of Vibration and Acoustics. 2013; 135(3). doi: 10.1115/1.4023812
31. Han DH, Zhao JB, Zhang GJ, Yao H. Study on low-frequency band gap characteristics of a new Helmholtz type phononic crystal. Symmetry. 2021; 13(8): 1379. doi: 10.3390/sym13081379
32. Wu LY, Chen LW. Wave propagation in a 2D sonic crystal with a Helmholtz resonant defect. Journal of Physics D: Applied Physics. 2010; 43(5): 055401. doi: 10.1088/0022-3727/43/5/055401
33. Yang A, Li P, Wen Y, et al. Enhanced Acoustic Energy Harvesting Using Coupled Resonance Structure of Sonic Crystal and Helmholtz Resonator. Applied Physics Express. 2013; 6(12): 127101. doi: 10.7567/apex.6.127101
34. Tamaki H, Kita H, Kobayashi S. Multi-objective optimization by genetic algorithms: A review. In: Proceedings of the IEEE Conference on Evolutionary Computation; 20–22 May 1996; Nagoya, Japan. pp. 517–522.
35. Conn AR, Gould N, Toint P. A Globally Convergent Augmented Lagrangian Barrier Algorithm for Optimization with General Inequality Constraints and Simple Bounds. Mathematics of Computation. 1997; 66(217): 261–288.
36. Panahi E, Hosseinkhani A, Frangi A, et al. A novel low-frequency multi-bandgaps metaplate: Genetic algorithm based optimization and experimental validation. Mechanical Systems and Signal Processing. 2022; 181: 109495. doi: 10.1016/j.ymssp.2022.109495
37. Weile DS, Michielssen E. Genetic algorithm optimization applied to electromagnetics: A review. IEEE Transactions on Antennas and Propagation. 1997; 45(3): 343–353. doi: 10.1109/8.558650